Voltage-Gated 90° Switching of Bulk Perpendicular Magnetic Anisotropy in Ferrimagnets

Zhengyu Xiao Ruiwen Xie, Fernando Maccari, Philipp Klaßen, Benedikt Eggert, Di Wang, Yuting Dai, Raquel Lizárraga, Johanna Lill, Tom Helbig, Heiko Wende, Kurt Kummer, Katharina Ollefs, Konstantin P Skokov, Hongbin Zhang, Zhiyong Quan, Xiaohong Xu, Robert Kruk, Horst Hahn, Oliver Gutfleisch, and Xinglong Ye*

ABSTRACT: Unraveling the mechanism behind bulk perpendicular magnetic anisotropy (PMA) in amorphous rare earth-transition metal films has proven challenging. This is largely due to the inherent complexity of the amorphous structure and the entangled potential origins arising from microstructure and atomic structure factors. Here, we present an approach wherein the magneto-electric effect is harnessed to induce 90° switching of bulk PMA in Tb−Co films to in-plane directions by applying voltages of only −1.2 V. This manipulation is achieved by voltage-driven insertion of hydrogen atoms into interstitial sites between Tb and Co atoms, which serves as a perturbation to the local atomic structure. Using angle-dependent X-ray magnetic circular dichroism, we find that the anisotropy switching originates from the distortion of the crystal field around Tb, which reorients the alignment of Tb orbital moments. Initially aligned along Tb−Co bonding directions, the easy magnetization axis undergoes reorientation and switches by 90°, as substantiated by ab initio calculations. Our study not only concludes the atomic origin of Tb−Co atom bonding configuration in shaping bulk PMA but also establishes the groundwork for electrically programmable ferrimagnetic spintronics, such as controlling domain wall motion and programming artificial spin textures.

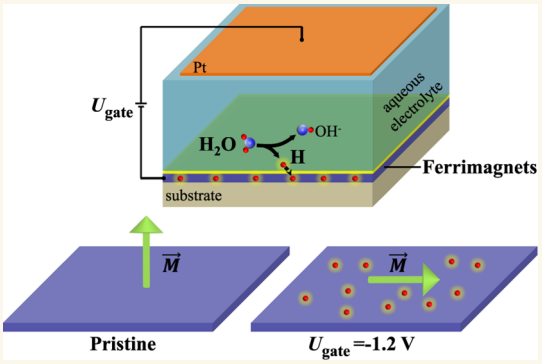

KEYWORDS: *perpendicular magnetic anisotropy, 90° switching, ferrimagnets, voltage, hydrogen atoms*

INTRODUCTION

Ferrimagnets, which combine the advantages of both ferromagnets and antiferromagnets—namely controllable magnetization and antiferromagnetic-like fast dynamics—have driven the rapid emergence of ferrimagnetic spintronics.[1] Among ferrimagnetic materials, amorphous rare earth-transition metal (RE-TM) ferrimagnetic films exhibit extraordinary properties, including ultrafast domain wall movement,[2,3] field-free magnetization reversal,[4] bulk Dzyaloshinskii−Moriya interaction,[5] nanoscale skyrmions,[6] flipping handedness of magnons,[7] and femtosecond optical switching.[8−10] These properties exploit the unique advantage of bulk perpendicular magnetic anisotropy (PMA) in amorphous ferrimagnetic films, i.e., a preferred magnetization orientation along out-of-plane directions in films even with large thickness (e.g., 500 nm).[11,12] While the discovery of PMA dates back to 1973, its manifestation in amorphous materials raises fundamental questions about its origin. Intrinsically, the local magnetic anisotropy originates from the interaction between aspherically distributed 4f electrons of RE ions, characterized by strong spin−orbital coupling, and the surrounding aspherical crystal field. In crystalline materials, the alignment of this local anisotropy with long-range crystal symmetries gives rise to macroscopic magnetic anisotropy, as seen in high-performance permanent magnets such as $SmCo_5$ and $Nd_2Fe_{14}B$.[13,14] However, in amorphous alloys, which lack crystal symmetry, the local single-ion anisotropy of RE ions

exhibits variations in both directions and magnitudes from site to site, effectively canceling out at macroscopic scales.[15]

Understanding the origin of bulk PMA has been hindered by the inherent difficulty of determining precise atomic positions and structure within an amorphous structure.[16,17] Proposed models to explain bulk PMA encompass both extrinsic microstructure and intrinsic atomic structure factors, such as columnar morphology,[18] composition inhomogeneity,[19] magneto-elastic effect,[20] pair-order anisotropy,[21,22] dipolar effect,[23] and bond-orientation anisotropy.[24] However, the exact mechanism governing PMA remains elusive. This is largely because conventional approaches to modulating bulk PMA energy, such as altering magnetron sputtering parameters, often result in concomitant changes of multiple microstructural and atomic-scale features. This complicates the interpretation of the experimental results. Disentangling effectively these changes and separating their effects on bulk PMA can be the key to resolving the mechanism of bulk PMA.

Recent studies have demonstrated that magnetic properties of materials, including magnetic anisotropy, coercivity, and Curie temperatures, can be controlled by applying small voltages, as exemplified in many ferro-/ferri-magnetic materials.[25−34] Unlike sputtering techniques, the magneto-electric approach modifies magnetism through mechanisms of electron doping or migration of ions (magneto-ionics), which usually do not change the microstructure of materials. In particular, we showed that the magnetic properties of ferromagnetic intermetallics even at the micrometer scale can be substantially modulated through electrochemically controlled insertion and extraction of hydrogen atoms in the metal structure.[35,36] Unlike electrons and ions, hydrogen atoms are electrically neutral, and therefore, their diffusion into the metal structure is not restricted by electric-field screening. This enables the control of bulk magnetic properties with small voltages. Moreover, hydrogen insertion into interstitial sites distorts the atomic structure while preserving the microstructure of materials, such as grain sizes and phase distributions.[32,33] In the case of amorphous ferrimagnets, we expect that hydrogen insertion into interstitial sites will not change the microstructural features such as column texture, roughness, geometry, spatial distribution of elements, and thickness at the micro/nanometer scale. This capability thus enables the disentanglement of the effects of the microstructure on bulk PMA, providing insights into the atomic origin of bulk PMA. In this work, we employed the newly developed voltage-driven hydrogen insertion/extraction approach to modify bulk PMA in amorphous ferrimagnets. We show that by applying voltages as small as −1.2 V, bulk PMA of amorphous ferrimagnetic TbCo films can be switched completely by 90° to in-plane directions. This yields a voltage-controlled huge modification of coercivity by 2.0 T at room temperature, the largest ever achieved by magneto-electric approaches. Through angle-dependent X-ray magnetic circular dichroism (XMCD), we find that upon hydrogen insertion, Tb orbital moments, which determine the single-ion magnetic anisotropy, reorient from out-of-plane direction to in-plane directions due to the distortion of the crystal field. As verified by ab initio calculations, the easy axis of magnetization initially aligns along Tb−Co bonding directions but reorients and switches their directions due to the presence of interstitial hydrogen atoms. Our findings conclude the long-standing question of the atomic origin of bulk PMA in amorphous ferrimagnets. Moreover, the ability to manipulate PMA with small voltages of about 1 V holds great promise for significantly advancing electrically programmable ferrimagnetic spintronics.

RESULTS AND DISCUSSION

We used amorphous TbCo thin films as our model material, renowned for their large bulk PMA.[37,38] Thin films were deposited onto thermally oxidized Si substrates by magnetron cosputtering of Tb and Co elements (purity 99.9%) at room temperature, with thicknesses of 20, 50, and 500 nm. Compositions were adjusted by varying sputtering powers, which lead to magnetization compensation temperatures (T_M) from 200 K to above room temperature. We further deposited 5 nm-thick Pd layers onto TbCo films to avoid sample oxidation, which also facilitates the passage of hydrogen atoms. To control insertion of hydrogen atoms in TbCo films, we utilized an electrochemical setup with three electrodes (Figure 1A), i.e., the working electrode (WE, Pd/TbCo/Si), the counter electrode (CE, Pt foil), and the reference electrode (Hg/HgO electrode, not shown for clarity). The electrolyte is 1 M KOH aqueous electrolyte (shaded by light green color). When a gate voltage (−1.2 V) was applied between the working electrode and the counter electrode across the electrolyte, water molecules were reduced into hydrogen

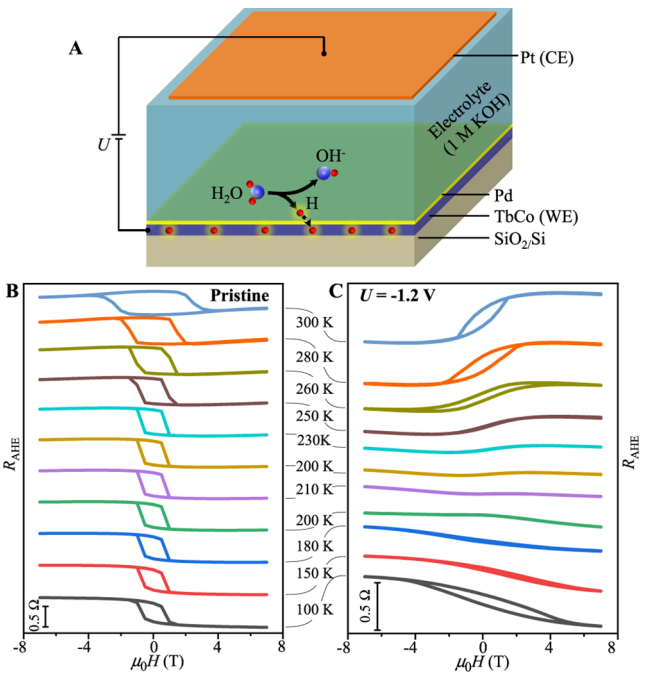

Figure 1. Voltage-driven 90° switching of bulk PMA to in-plane directions in Tb−Co ferrimagnetic films (T_M > 300 K). (A) Schematic of an electrochemical setup used for voltage-driven hydrogen insertion and the sample configuration of Pd/TbCo/SiO_2/Si. When −1.2 V is applied between the working electrode (WE, TbCo layer) and the counter electrode (CE, Pt foil) across the electrolyte (1 M KOH aqueous solution), water molecules will be reduced into OH^- and hydrogen atoms (H) on the surface of Pd layers. Driven by gradient of concentration, hydrogen atoms will sequentially diffuse into Pd and TbCo layers. (B) Hysteresis loops of anomalous Hall resistance for as-grown thin films and (C) for those after applying −1.2 V, measured at temperatures from 300 to 100 K. Note the 90° switching of magnetic anisotropy and the reduction of T_M from initially above 300 K to about 210 K after hydrogen insertion. Magnetic fields were applied along out-of-plane directions.

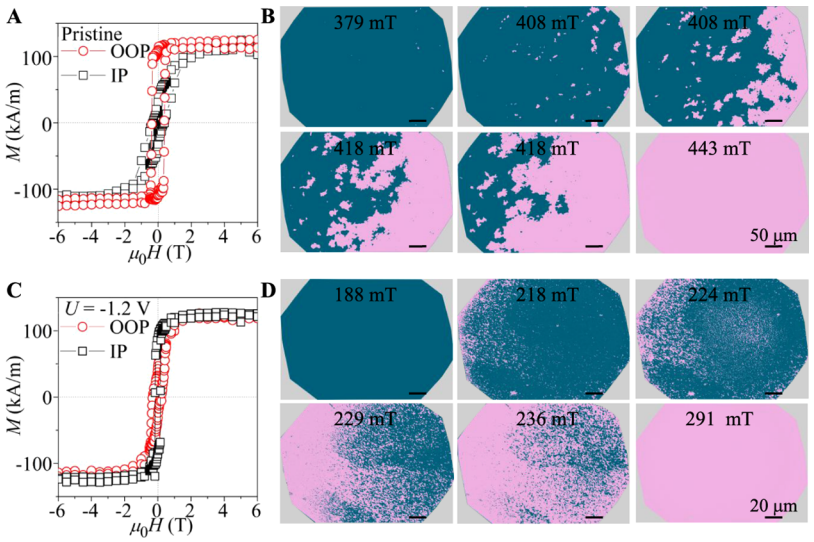

Figure 2. Magnetization behavior in Tb−Co ferrimagnetic films (T_M ~ 200 K) before and after applying −1.2 V. (A) Magnetic hysteresis loops of as-grown films measured at room temperature along out-of-plane and in-plane directions, evidencing the robust PMA. (B) The corresponding MOKE images of magnetic domain structure under increasing magnetic fields applied along out-of-plane directions. Note the nucleation and displacement of magnetic domain walls under constant magnetic fields of 408 and 418 mT. (C) Magnetic hysteresis loops of TbCo films after the application of −1.2 V at room temperature, demonstrating 90° anisotropy switching in comparison with (A). (D) The corresponding MOKE images of magnetic domain structure after applying −1.2 V, showing the gradual formation of isolated, interspersed domains. Low-temperature magnetic hysteresis loops are shown in Figure S4.

atoms that initially adsorb onto the Pd surface. Driven by the gradient of concentration, they diffuse then into the Pd layer and subsequently into the TbCo layer. Notably, the mixing enthalpy of hydrogen atoms and TbCo is more negative than that of hydrogen and Pd.[39,40] Consequently, hydrogen atoms exhibit unidirectional diffusion from Pd to TbCo layers, ensuring the nonvolatile and irreversible retention of voltage-driven hydrogen insertion within TbCo layers. This irreversibility facilitates subsequent characterization of magnetic properties, electron transport, and magnetic moments under high vacuum and at low temperatures.

As-grown TbCo thin films exhibit typical PMA at various temperatures, evidenced by the rectangular out-of-plane hysteresis loops probed by the anomalous Hall effect (AHE) (Figure 1B). At 300 K, the polarity of AHE resistance remains negative under a positive magnetic field, indicating the compensation temperature T_M above 300 K (with nominal composition $Tb_{45}Co_{55}$).[41] In comparison, upon applying −1.2 V, T_M decreased substantially to about 210 K, signified by the inversion of AHE polarity (Figure 1C). As a result, the coercivity at room temperature changes from 2.5 to 0.5 T, representing an unprecedented voltage-induced coercivity manipulation by 2 T. Most importantly, we observed that after applying −1.2 V, the AHE hysteresis loops exhibited the hard axis behavior with tilted shapes under out-of-plane magnetic fields, indicating the 90° switching of magnetic anisotropy from PMA to in-plane directions. Likewise, we have observed similar voltage-driven anisotropy switching for other TbCo thin films with initial T_M of 200 K (Figures S1 and S2) and 295 K (Figure S3).

Magnetometry measurements validate the voltage-driven anisotropy switching through directly measuring magnetization behaviors along both the out-of-plane and in-plane directions on TbCo thin films (initial T_M of 200 K). Figure 2A,C shows the magnetic hysteresis loops of TbCo samples before and after applying −1.2 V at room temperature (for measurements at low temperatures, please see Figure S4). By comparing hysteresis loops along the two directions, it is clear that the as-grown sample exhibits the typical PMA, in agreement with AHE measurements (Figures S1 and S2). In contrast, after applying −1.2 V, the magnetic hysteresis loops interchanged their shapes along two directions, with the in-plane loop now displaying the rectangular shape (Figure 2C). This verifies the reorientation of the magnetic anisotropy from the perpendicular to the in-plane direction. With the measured values of 5 T for the anisotropy field (H_a), the anisotropy energy was calculated to be 0.5 MJ/m^3 at 100 K using the relation $K_U = {}^1/_2 H_a M_S + {}^1/_2 \mu_0 M_S^2$ (see Supporting Information), indicating the giant magnetoelectric efficiency. Note that the magnetization drop at low magnetic fields for all samples can be attributed to the Tb-rich layer near the substrate (Figures S5 and S6).

Another intriguing feature induced by voltage-driven anisotropy switching is the atypical magnetization reversal process observed by magneto-optical Kerr effect (MOKE) microscopy. For as-grown samples, the reversed magnetic domains nucleate at multiple positions from the fully magnetized state and then propagate into neighboring regions (Figure 2A,B). These reversed domains have fractal, irregular boundaries and creep fast into nonreversed regions under constant magnetic fields, a phenomenon known as the magnetic aftereffect.[42] In contrast, after voltage-driven hydrogen insertion, magnetization reversal proceeds predominantly through point-by-point reversals of interspersed magnetic domains (Figure 2C,D). Those domains exhibit no further growth, and under increasing fields, more individual reversed domains occur until the full reversal of magnetization.

These comprehensive AHE, magnetometry, and MOKE measurements thus clearly demonstrate the ability to manipulate the magnetic anisotropy of ferrimagnetic thin films from perpendicular to in-plane directions by applying small voltages. This voltage-driven anisotropy switching

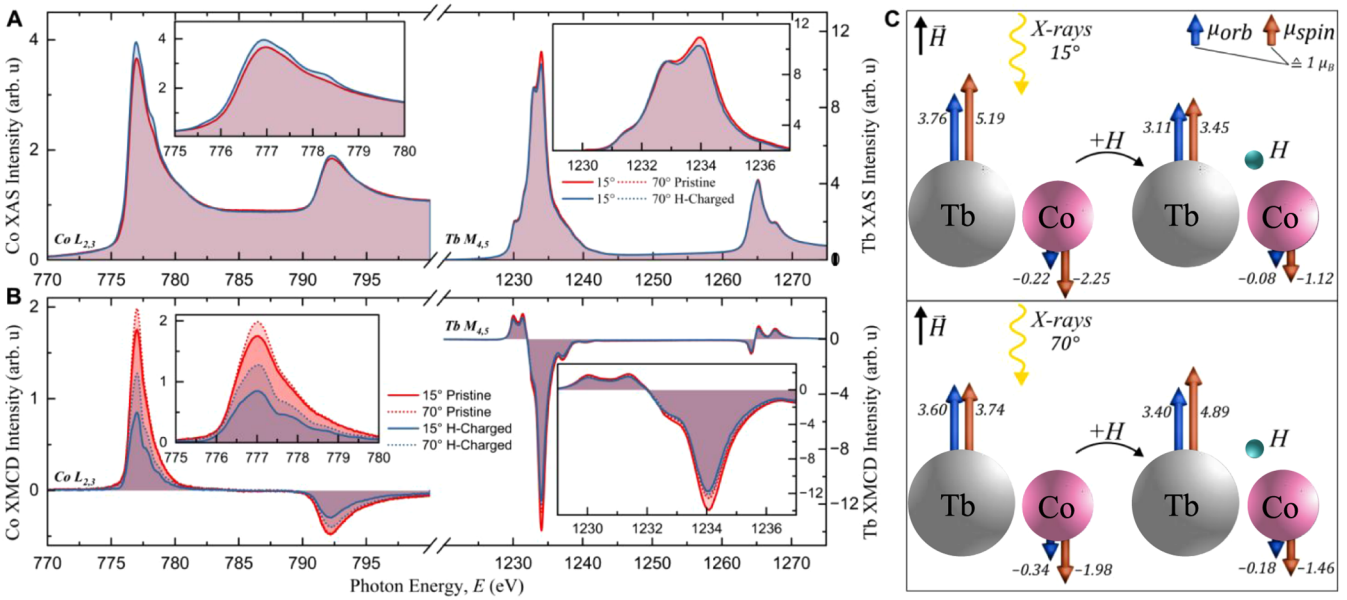

Figure 3. Angle-dependent XAS and XMCD spectra for TbCo ferrimagnetic films ($T_M \sim 295$ K) before (pristine) and after applying −1.2 V (H-Charged). (A) XAS spectra at Tb $M_{4,5}$ and Co $L_{2,3}$ edges for samples before and after hydrogen insertion, which resemble each other in terms of peak positions and line shapes. (B) The corresponding XMCD spectra for Co and Tb along both perpendicular and grazing incidence angles, showing the substantial dependence on incidence angles in accordance with magnetic anisotropy. (C) The resolved spin and orbital moments of Co and Tb by sum rules, showing the opposite dependence of Tb orbital moments on incidence angles. The given numbers of the moments are in the units of μ_B/atom. All measurements were performed at T = 5 K, with an applied magnetic field of 8 T parallel to the incoming photon beam, and perpendicular and grazing angles are 15° and 70° with respect to the surface normal of thin films.

therefore presents a unique opportunity to probe the origin of PMA by elucidating the structural changes induced by hydrogen insertion. Our investigation commenced with microstructure characterization. Transmission electron microscopy (TEM) reveals that after hydrogen insertion, TbCo thin films maintain their homogeneous morphology without forming cracks or substructures (Figure S5). Energy dispersive X-ray spectroscopy (EDS) mapping shows inhomogeneous distributions of Tb and Co atoms, typical of amorphous thin films sputtered at room temperature,[5,43] but no discernible differences were detected before and after hydrogen insertion (Figures S6 and S7). Hydrogen distribution can be inhomogeneous with potentially higher concentration near the Pd/TbCo and TbCo/substrate interfaces. This is due to the nonuniform distribution of Tb elements, which tend to segregate at these interfaces (Figure S6 and S7). However, hydrogen segregation is confined to about 2 nm near the interfaces, and its effect on magnetic anisotropy is likely insignificant, as the phenomenon of voltage-driven anisotropy switching has been observed even in thick films (500 nm). Selected area electron diffraction (SAED, Figure S5) and macroscopic X-ray diffraction (XRD, Figure S8) confirm the maintenance of the amorphous structure after voltage-driven hydrogen insertion, with broad, diffusive diffraction peaks/halos. These results align with our anticipation that hydrogen insertion into interstitial sites between Tb and Co atoms will not change the microstructural features. Moreover, the magnetic anisotropy of RE-TM alloys, as mentioned earlier, originates from the interaction between strongly spin−orbit-coupled, aspherically distributed 4f electrons in rare earth elements and the surrounding crystal field created by neighboring atoms. It is considered that the 4f electrons are deeply localized and shielded from the external environment, making them less susceptible to changes in external environmental changes. Given this, the anisotropy switching from PMA to in-plane directions is more likely attributed to the distortion of the crystal field surrounding the Tb atoms.

Given the inherent difficulty of directly resolving the atomic structure and its distortion in amorphous materials, we probed the electronic structure and magnetic moments of Tb and Co through element-specific X-ray absorption (XAS) and XMCD measurements.[44] These measurements were conducted along both grazing and normal directions (15° and 70° with respect to the surface normal) on TbCo films (initial T_M of 295 K, Figure S4). Figure 3A shows that the XAS spectra measured at Co $L_{2,3}$ edges and Tb $M_{4,5}$ possess no significant changes in line shapes and peak positions before and after hydrogen insertion, indicating the unchanged metallic character for Co[45,46] and the Tb^{3+} states.[47] However, the appearance of the spectral fine structures at Co L_3 white line and a small shift toward lower energies (see inset of Figure 3A) after hydrogen insertion suggests the presence of interstitial hydrogen near Co atoms.

We resolved the spin and orbital moments of Tb and Co elements by applying magneto-optical sum rules to the XMCD spectra (Figure 3B,C).[48,49] For the Tb $M_{4,5}$ edges, we used ab initio calculations to calculate the contribution from the magnetic dipole operator $\langle T_z \rangle$, which can be significant in RE elements in contrast to transition metals. The values obtained are $\langle T_z \rangle$ = 0.20 (0) for 15° and 0 (0.21) for 70° for as-grown (hydrogen-charged) samples, which agree well with the values calculated in the literature.[50] We refer the reader to the Supporting Information for detailed discussions of the obtained $\langle T_z \rangle$ term and sum rule analysis (Figures S9−S11). As outlined in Figure 3C and Table S1, the total magnetic moment of the Co atom in the as-grown samples is −2.5 μ_B consistent with XMCD results for other amorphous RE-Co compounds.[51] The large magnitude of the Co moment might

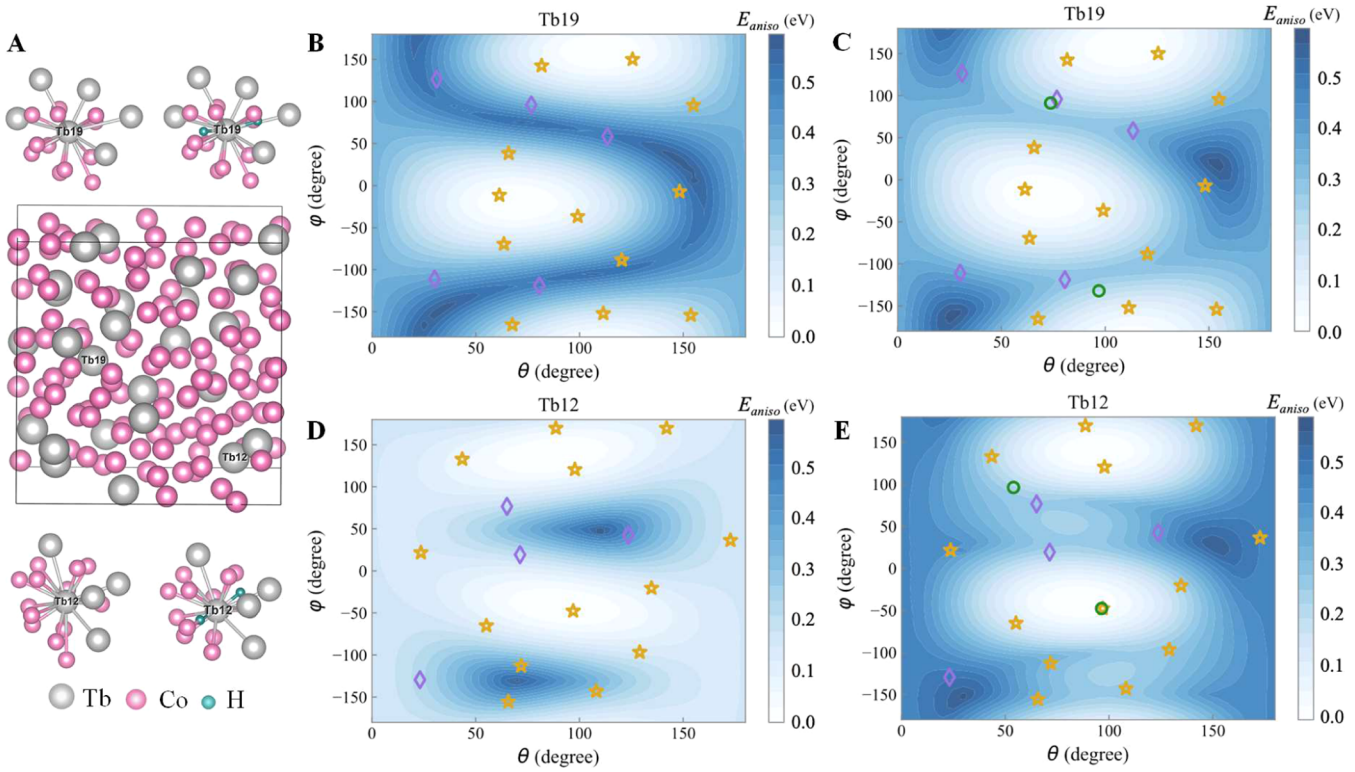

Figure 4. Ab initio calculations of three-dimensional magnetic anisotropy contour in TbCo atom configuration before and after hydrogen insertion. (A) The supercell structure to simulate the amorphous structure of TbCo built through stochastic quenching. The spatial directions and vectors of Tb−Tb and Tb−Co bonding were projected in spherical coordinate with polar and azimuth angles (θ, φ). Top and bottom panels show two representative clusters centered around Tb atoms (Tb12 and Tb19). (B) Contour maps of E_{aniso} plotted against θ and φ for Tb19, showing the high anisotropy energy along Tb−Tb direction (diamond symbols on the blue arc). (C) Contour maps of E_{aniso} plotted against θ and φ for Tb19 after hydrogen insertion, showing the substantial weakening of the anisotropy difference between Tb−Co and Tb−Tb bonding directions. (D) Contour plot of magnetic anisotropy energy around Tb12 before and (E) after hydrogen insertion, evidencing the 90° reorientation of anisotropy direction due to hydrogen insertion.

be associated with the increased bond distances in amorphous alloys as compared to *hcp*-Co. For Tb, the total magnetic moment and the orbital moment are 8.9 μ_B and 3.7 μ_B, matching the expected values for the $4f^8$ configuration and consistent with previously reported data.[51] Upon hydrogen insertion, the magnetic moments of both Tb and Co decreased substantially by 35% and 50%, respectively (Figure 3C), which are associated with the observed decrease of T_M. Of particular interest is the angle dependence of the magnetic moments of Tb before and after hydrogen insertion, which are directly related to magnetic anisotropy according to the RE single-ion anisotropy model. For the as-grown samples, we observed larger magnetic moments and orbital moments of Tb in perpendicular directions compared to grazing incidence directions. This phenomenon, i.e., orbital moments of RE atoms are larger along perpendicular directions than grazing directions, has also been observed in amorphous NdCo films with large PMA.[51] However, after hydrogen insertion, the opposite was observed, i.e., the Tb orbital moments become larger along the grazing angle than along perpendicular directions. This indicates the reorientation of local magnetic anisotropy at the atomic scale and the change of the crystal field around Tb. It is worthwhile to note that, due to the limited probing depth of XMCD measurements in total electron yield mode (<10 nm), the magnetic moments obtained from XMCD analysis may differ from those of the entire films, as Tb elements tend to segregate near the surface. However, since bulk PMA and the voltage-driven anisotropy switching have been observed throughout the entire films, the trend in how magnetic moments change along two directions before and after hydrogen insertion is expected to remain consistent.

We noted that although the magnetic moments of Tb and Co at 5 K, as obtained from XMCD, decrease substantially after hydrogen insertion, the overall saturation magnetization measured at 300 K via magnetometry remains almost unchanged (Figure 2A,C). This discrepancy can be attributed to three factors. First, XMCD probes the element-specific magnetic moment of Tb and Co atoms, whereas magnetometry measures the net magnetization associated with the difference between Tb and Co moments. Consequently, when both Tb and Co moments decrease, their net subtraction may exhibit a less pronounced decrease. Second, due to antiferromagnetic ordering of Tb and Co moments, the net saturation magnetization of TbCo films depends strongly on the temperature relative to their compensation temperatures. The T_M for the pristine samples and those after hydrogen insertion are 198 and 130 K, respectively (Figures 2 and S2). When measured at 300 K, the pristine samples are closer to their compensation temperatures than those after hydrogen insertion. As a result, the net magnetization of the pristine samples decreases more significantly, making their values comparable to those after hydrogen insertion. Third, XMCD primarily probes the near-surface region with a typical penetration depth of less than 10 nm, whereas magnetometry measures the entire films. In our cases, Tb elements tend to

segregate at surfaces, leading to differences in the composition of the near-surface region compared to the overall film. This distinction in measurement techniques further complicates the direct comparison between the XMCD and magnetometry results. Given these factors, we primarily use magnetometry to verify the voltage-driven anisotropy switching since it can measure magnetization from both perpendicular and in-plane directions. In addition, we used XMCD to probe the spin and orbital moments of Tb and Co atoms, providing insights into the changes in their electronic environment induced by interstitial hydrogen atoms. We also notice that the obtained anisotropy in magnetic moments of Tb and Co, measured along two different angles by XMCD, is relatively larger than that obtained from magnetometry measurements. In the latter case, saturation magnetization along the hard axis can approach that along the easy axis, especially at 300 K (Figures 2A,G and S4). This difference can be again caused by the distinction between XMCD and magnetometry techniques, which measure the near-surface regions and the overall films, as well as the strong dependence of the magnetic moments on temperatures.

To elucidate the distortion of the crystal field and the corresponding anisotropy switching at the atomic scale induced by hydrogen insertion, we acquired the three-dimensional mapping of magnetic anisotropy in amorphous TbCo and TbCo-H structures by ab initio calculations. The amorphous TbCo structure was simulated by constructing a 150-atom supercell with 25 Tb and 125 Co atoms using stochastic quenching (Figures 4A and S12).[52,53] The single-ion anisotropy of each Tb atom was evaluated by solving its atomic Hamiltonian, including Coulomb interactions ($\hat{H}_U$), spin−orbit coupling (SOC), crystal field Hamiltonian ($\hat{H}_{CF}$), and the exchange coupling term resulting from the magnetization of Co atoms ($\hat{H}_{ex}$):

$$\hat{H}_{at} = \hat{H}_U + \lambda \sum_i \hat{s}_i \hat{l}_i + \hat{H}_{CF} + \hat{H}_{ex}$$

In particular, the crystal field parameter $\hat{H}_{CF} = \sum_{k=0}^{k_{max}} \sum_{q=-k}^{k} B_q^{(k)} \hat{C}_q^{(k)}$ was obtained by transforming the Tb 4f band states calculated by density functional theory (DFT) to Wannier functions, which were expanded with crystal field parameters (CFPs) $B_q^{(k)}$ in a series of spherical tensor operators $\hat{C}_q^{(k)}$.[54] Subsequently, we evaluated the magnetic anisotropy ($E_{aniso} = E_{eigen} - E_{eigen}^{min}$) by calculating the eigenvalue (E_{eigen}) of $\hat{H}_{at}$ with magnetization directions defined by polar angle θ ([0, π]) and azimuth angle φ ([$-\pi$, π]).

Analyzing the correlations between E_{aniso} and Tb−Tb/Tb−Co bonding directions, we found that the easy magnetization directions are statistically aligned along the Tb−Co bonding directions (Figure S13). This feature persists across various compositions, for instance, $TbCo_4$ (Figure S13). Figure 4B,D shows the contour plots of E_{aniso} against θ and φ for two Tb atoms (indexed as Tb12 and Tb19) among 25 Tb atoms, along with the angular projections of Tb−Co and Tb−Tb bonding vectors. It is evident that the low/high E_{aniso} zones, i.e., the easy/hard magnetization directions, significantly overlapped with the Tb−Co/Tb−Tb bonding directions. This important finding pinpoints the critical role of the Tb−Co bonding direction in shaping PMA. Previously, Harris et al. observed in TbFe thin films that the Fourier-transformed density of TbFe nearest neighbor pairs along the out-of-plane direction is slightly larger (1−4%) than along in-plane directions, thereby leading to the phenomenological model of pair-order anisotropy.[21,22] However, doubts remain about how the PMA arises at the atomic scale and whether such minor anisotropy can induce such high PMA.[55] Our finding, for the first time, reveals the preference of magnetization along Tb−Co directions at the atomic scale. Most compellingly, upon hydrogen insertion as a perturbation, the initially high E_{aniso} zone (Tb−Tb directions) decreased to values comparable to those along the Tb−Co directions, thereby substantially weakening the magnetic anisotropy (Figure 4C). Remarkably, for the atom configurations of Tb12, the crystal field parameter B_2^0 changed its sign from positive to negative values upon hydrogen insertion (Figure 4E), which causes a 90° reorientation of the easy magnetization axis (Figures S14 and S15 and Table S2).[56,57] This result reproduced the experimentally observed 90° anisotropy switching, indicating the representative atom configuration for large PMA. These theoretical calculations, using interstitial hydrogen atoms as a perturbation to the atomic structure, thus clarify the distortion of the crystal field around Tb in switching PMA, as experimentally observed.

CONCLUSION

In summary, by combining experimental and theoretical approaches, we explored the atomic origin of bulk PMA in amorphous ferrimagnetic films. To disentangle the effect of microstructure, we employed the recently developed magneto-electric approach of voltage-driven insertion of hydrogen atoms into interstitial sites, which acts as a perturbation to the local atomic structure. Remarkably, we show that by applying only −1.2 V, the bulk PMA can be switched by 90° to in-plane directions in TbCo films. This enables the unprecedented change of coercivity by 2.0 T at room temperature and the evolution of interspersed magnetic domain structures observed for the first time in ferrimagnets. Analyzing the anisotropy-switching process, angle-dependent XMCD reveals the loss of preferential orientation of Tb orbital moments, which determines the single-ion anisotropy of the Tb atoms. As verified by ab initio calculations, the easy magnetization axis originally aligns along Tb−Co bonding directions but reorients and switches by 90° due to the distorted crystal field. Our study disentangles the effect of microstructure and atomic structure on bulk PMA, identifying the decisive role of the Tb−Co atom configuration in shaping PMA. An exceptionally large PMA may thus be anticipated by depositing sequential layers of RE and TM elements, magnifying the population of Tb−Co bondings along perpendicular directions. Moreover, our work opens up a previously inaccessible route to manipulating local PMA in ferrimagnetic films by applying small voltages. This lays the groundwork for broad applications in the rapidly emerging field of ferrimagnetic spintronics,[1−10] such as controlling domain-wall movement, skyrmion sizes, and magnon propagation. The ability to engineer local magnetic anisotropy with ultralow voltages also enables the development of electrically programmable artificial spin textures in ferrimagnets, such as those with alternating in-plane and out-of-plane magnetization as building blocks.[58,59]

EXPERIMENTAL METHODS

Growth of Thin Films. Amorphous TbCo thin films were deposited by DC magnetron cosputtering of Tb and Co targets at room temperature. Considering that the PMA is bulk magnetic anisotropy, we deposited thin films directly onto a

thermally oxidized Si substrate without using buffer layers. The background pressure of the sputtering chamber was $<9 \times 10^{-8}$ mbar, and the Ar pressure was 3 mbar during deposition. The TbCo compositions were adjusted by varying the Tb sputtering power to tune the Tb deposition rate. The layer thicknesses and nominal alloy atomic compositions were determined by EDS and TEM. A 5 nm Pd layer was deposited onto the TbCo layer as a capping layer, which prevented the oxidation of the Tb−Co layer and allowed the transport of hydrogen atoms into the TbCo layer during voltage-driven hydrogen insertion. For XMCD measurements, we used a Pd capping layer with a smaller thickness of 2 nm to increase the electron yield from the TbCo layers.

Magnetometry, AHE, and MOKE Characterizations. Magnetometry measurements were performed in a superconducting quantum interference device (SQUID, MPMS3) at different temperatures with magnetic fields applied along both the out-of-plane and in-plane directions. The magnetic hysteresis loops of TbCo layers were obtained by subtracting the linear diamagnetic contribution of the Si substrate from the measured magnetization. The anomalous Hall effect (AHE) measurements were performed in PPMS at different temperatures by utilizing the van der Pauw method. The samples were cut into square shapes with a size of approximately 4 × 4 mm. The AHE mostly arises from the Co sublattice, and thus, its polarity allowed us to determine the magnetically dominant sublattice. The evolution of the magnetic domain structure during the magnetization reversal process was characterized by a magneto-optical Kerr effect (MOKE) microscope (Zeiss Axio Imager, D2m evico magnetics GmbH, wavelength 660 nm) under magnetic fields using both polar and longitudinal modes. To enhance the image contrast, the nonmagnetic background image was subtracted from the collected average image using KerrLab software.

Electrochemical Charging of Hydrogen Atoms. Voltage-driven hydrogen insertion into TbCo films was carried out under potentiostatic control in a three-electrode electrochemical system (Autolab PGSTAT 302N). The working, counter, and reference electrodes were Tb−Co thin films, Pt wires, and a pseudo Ag/AgCl electrode, respectively, within the homemade electrochemical cell in PPMS. To charge the thin film, we used a potential of −1.2 V for a short duration of about 2 min. The potential of the pseudo Ag/AgCl electrode is 0.300 ± 0.002 V more positive than the standard Hg/HgO (1 M KOH) electrode, and all potentials in the paper were with reference to the Hg/HgO (1 M KOH) electrode. The electrolyte was an aqueous electrolyte of 1 M KOH prepared from ultrapure water with a resistivity of ∼18.2 MΩ cm.

TEM Characterization. The microstructures of amorphous thin films were characterized by TEM and selected area diffraction (TEM, FEI Titan 80-300) equipped with EDS. Preparation of TEM samples followed the procedure of cutting, lifting, and milling using an FIB/SEM dual beam system (FEI Strata 400 and Zeiss Auriga 60, KIT). Radial distribution functions of elements were obtained by Fourier transformation of the selected area diffraction pattern collected at least at four different positions.

XMCD Measurements. X-ray absorption spectroscopy (XAS) and X-ray magnetic circular dichroism (XMCD) experiments were performed at the ID32 beamline of the European Synchrotron Radiation Facility (ESRF, Grenoble, France) by measuring absorption spectra at the Co $L_{2,3}$ and Tb $M_{4,5}$ edges. All spectra were recorded using the total electron yield detection mode. The isotropic XAS spectra were approximated by averaging XAS spectra measured with right and left circularly polarized X-rays and under a constant magnetic field of 8 T, whereas XMCD spectra were obtained as their difference. All spectra for each sample before and after voltage-driven hydrogen insertion were measured at two different sample orientations, i.e., at normal (15°) and grazing angles (70°) with respect to the normal of the sample surface. The expectation values for the spin and orbital moments of Co and Tb were calculated by using the following dichroism sum rules:

$$\langle S_z^{\mathrm{Co}} \rangle = (10-n)\frac{\int_{L_3} \mathrm{d}\omega\,(\mu^+ - \mu^-) - 2\int_{L_2} \mathrm{d}\omega\,(\mu^+ - \mu^-)}{\int_{L_{2,3}} \mathrm{d}\omega\,(\mu^+ + \mu^-)} - \frac{7}{2}\langle T_z \rangle$$

$$\langle L_z^{\mathrm{Co}} \rangle = (10-n)\frac{4}{3}\frac{\int_{L_{2,3}} \mathrm{d}\omega\,(\mu^+ - \mu^-)}{\int_{L_{2,3}} \mathrm{d}\omega\,(\mu^+ + \mu^-)}$$

$$\langle S_z^{\mathrm{Tb}} \rangle = (14-n)\frac{\int_{M_5} \mathrm{d}\omega\,(\mu^+ - \mu^-) - \frac{3}{2}\int_{M_4} \mathrm{d}\omega\,(\mu^+ - \mu^-)}{\int_{M_{4,5}} \mathrm{d}\omega\,(\mu^+ + \mu^-)} - 3\langle T_z \rangle$$

$$\langle L_z^{\mathrm{Tb}} \rangle = (14-n)2\frac{\int_{M_{4,5}} \mathrm{d}\omega\,(\mu^+ - \mu^-)}{\int_{M_{4,5}} \mathrm{d}\omega\,(\mu^+ + \mu^-)}$$

where n is the number of occupied states in the outer shell and $\langle T_z \rangle$ is the expectation value for the magnetic dipole operator. For the extraction of the Co moments, we assumed $n = 2.49$,[60] and for simplicity, $\langle T_z \rangle = 0$. For Tb, we assumed $n = 8$ (Tb^{3+}). To derive the respective moments, we used the known relations $\mu_S = -2\langle S_z \rangle \mu_B$ and $\mu_L = -2\langle L_z \rangle \mu_B$. The expectation values $\langle T_z \rangle$ for the Tb atoms were calculated using ab initio calculations and averaged over all Tb atoms, and the calculated results are shown in Figure S9. The dependence of the magnetic moments on the $\langle T_z \rangle$ for the range of the calculated values is presented in Figure S10. It is known that $\langle S_z \rangle$ and $\langle T_z \rangle$ are antiparallel for Tb^{3+} ions, and consequently, only positive values were considered when $\langle S_z \rangle$ is negative. To account for the transitions into the continuum, we have deployed step functions and subtracted them from the measured X-ray absorption intensity to form the integrant $(\mu^+ + \mu^-)$ as the denominator in the above-formulated sum rules. The used step functions are shown in Figure S11.

Ab Initio Calculations. The stochastic quenching procedure for the construction of the 150-atom cell is as follows: an initial configuration of 150 atoms was generated by randomly distributing them in a cubic box with the constraint that the closest atom pair was 2.0 Å. The atomic coordinates were then relaxed using the Vienna ab initio simulation package (VASP) until the forces on every atom were smaller than 0.05 eV/Å.[61] The lattice parameter of the cubic cell was determined to be around 12.0 Å. In the VASP calculation, the 4f electrons of Tb were treated as core states. The calculation was performed at the Γ−k point with an energy cutoff of 350 eV. Two structures were constructed to simulate Tb−Co amorphous systems with different Co/Tb ratios, denoted as

$Tb_{25}Co_{125}$ and $Tb_{32}Co_{118}$ (see Figure S12A,C). To simulate the hydrogen-charged amorphous Tb−Co system, we added one extra hydrogen atom into each Tb-centered cluster in the pristine structures, denoted as $Tb_{25}H_{25}Co_{125}$ and $Tb_{32}H_{32}Co_{118}$, respectively (see Figure S11B,D).

In terms of the evaluation of crystal field parameters (CFPs), we followed the method proposed by Novák et al. that uses Wannier functions to construct the crystal field Hamiltonian: $\hat{H}_{CF} = \sum_{k=0}^{k_{max}} \sum_{q=-k}^{k} B_q^{(k)} \hat{C}_q^{(k)}$, where $\hat{C}_q^{(k)}$ is a spherical tensor of rank k acting on electrons in the 4f shell and the $B_q^{(k)}$ are CFPs. The calculation of CFPs consists of four steps:

(1) The self-consistent band calculation by treating 4f electrons of Tb as core states was performed to determine the single-particle potential of the Tb ion.

(2) The 4f states as well as Co 3d states (for hydrogen-charged systems the H 1*s* states as well) were treated as valence states in a nonself-consistent calculation while all other states were moved away using the orbital shift operator. In addition, a correction Δ that amounts to the downward shift of Co 3d (H 1s) level was introduced to approximate the actual charge transfer energy by modifying the difference $\epsilon_f - \epsilon_d$.

(3) The Tb 4f states were transformed to Wannier basis using the Wien2wannier[62] and Wannier90[63] packages. Wannier90 provides the atom-centered 7 × 7 matrix $\hat{H}_{4f}$, which is equivalent to $E_{avg}\hat{I} + \sum_{k,q} B_q^{(k)} \hat{C}_q^{(k)}$ with $E_{avg} = \mathrm{Tr}(\hat{H}_{4f}/7)$. The traceless part is then the desired crystal field Hamiltonian $\hat{H}_{CF}$.

(4) To get the standard form of CFPs, $\hat{H}_{4f}$ was transformed into the basis of spherical harmonics and expanded as a 49-dimensional vector in the basis of spherical tensor operators.

For the evaluation of CFPs, the optimized pristine and hydrogen-charged TbCo structures using VASP were employed, and the Tb atoms were assumed to possess the Tb^{3+} state. The steps (1) and (2) were carried out using the WIEN2k package with the implemented augmented plane waves + local orbital method.[64] The generalized-gradient approximation (GGA) was used as the exchange-correlation functional. We set $RK_{max} = 7.0$ for the Γ k point calculation. The atomic radii of Tb and Co were 2.23 and 1.98 Å, respectively. In step (2), the hybridization parameters Δ corresponding to Co 3d and hydrogen 1s states were taken as −0.6 and −1.4 Ry, respectively, to ensure that the Wannier functions of Tb 4f orbitals are located at the Tb atomic positions with very limited spread (smaller than 0.5 $Å^2$ in this case).

In order to evaluate the single-ion anisotropies (SIAs) of Tb, we constructed the atomic Hamiltonian of Tb by including the Coulomb interactions ($\hat{H}_U$), the spin−orbit coupling (SOC), the crystal field Hamiltonian ($\hat{H}_{CF}$), and the exchange coupling term resulting from the magnetization of Co atoms ($\hat{H}_{ex}$):

$$\hat{H}_{at} = \hat{H}_U + \lambda \sum_i \hat{s}_i \hat{l}_i + \hat{H}_{CF} + \hat{H}_{ex}$$

The eigenvalue of $\hat{H}_{at}$ (E_{eigen}) was solved using the Lanczos algorithm as implemented in the Quanty code,[65] which corresponds to the magnetic anisotropy energy (defined as $E_{eigen} - E_{eigen}^{min}$) by varying the magnetization direction represented by the polar angle θ ($[0, \pi]$) and the azimuth angle ($[-\pi, \pi]$). $\hat{H}_U$ was specified by the Slater parameters F^2 = 11.93, F^4 = 7.49, and F^6 = 5.39, which were taken from ref 66. F^0 follows the relation that $F^0 = U + F^2 \times 4/195 + F^4 \times 2/143 + F^6 \times 100/5577$. Here, we simply took $U = 0$ since it is the relative energy change with respect to the magnetization direction of more interest rather than the absolute eigenvalue of the Hamiltonian. Similarly, for $\hat{H}_{CF}$, the B_0^0 term was also omitted. The SOC strength λ of the Tb^{3+} atom was set to 0.221.[67] For $\hat{H}_{ex} = 2\mu_B B_{ex} n \cdot \hat{S}_f$ (where $\hat{S}_f$ is the spin of the Tb 4f shell), we assumed the magnitude of exchange field B_{ex} to be 310 T as reported in crystalline $TbCo_5$.[67] By solving the eigenfunctions of the Hamiltonian, we also obtained the expectation value of the magnetic dipole term, defined as $\hat{T} = \hat{S} - 3\hat{r}(\hat{r}\cdot\hat{S})$, in which $\hat{S}$ and $\hat{r}$ are spin and radial position operators, respectively. In addition, the variation of the eigenvalue as a function of (θ, φ) was examined under different B_{ex}, as illustrated in Figure S12. Clearly, despite the distinct energy levels, the shape of the curve, i.e., the energetically favored magnetization direction, is not influenced by the magnitude of B_{ex}. We also adopted the CFPs with Δ = −0.4 Ry for Co 3d states in $Tb_{25}Co_{125}$ for the evaluation of magnetic anisotropy, i.e., assumed stronger hybridization between Tb and Co. Similarly, the distributions of high- and low-energy zones are not affected.

For each Tb atom in the pristine and hydrogen-charged amorphous structures, we generate a contour plot for E_{aniso} as a function of θ and φ (see the videos in Supporting Information for $Tb_{25}Co_{125}$, $Tb_{25}H_{25}Co_{125}$, $Tb_{32}Co_{118}$, and $Tb_{32}H_{32}Co_{118}$). Centered at each Tb atom, its local chemical environment is represented by Tb−Co and Tb−Tb, and/or Tb−H bonding within cutoff radii of 3.5, 4.0, and 3.0 Å, respectively. Figure S12 offers a better visualization of the distributions of E_{aniso} in $Tb_{25}Co_{125}$ and $Tb_{32}Co_{118}$ along the directions corresponding to various chemical bonding since the distributions of E_{aniso} corresponding to Tb−Co bonding directions below the middle bar $(E_{aniso}^{min} + E_{aniso}^{max})/2$ are much denser than those above the middle bar. In addition, for a larger fraction of Tb atoms, the Tb−Tb bonding directions are located either right along or close to the hard magnetization directions.

The CFPs of Tb12 in both pristine and hydrogenated structures are given in Table S2. In order to investigate which parameter is mainly responsible for the change of anisotropy displayed in Figure 4 D and E, we have separately checked how the variations of dominating CFPs B_2^0, B_4^0, B_6^0, and B_6^6 influence the shape of the magnetic anisotropy. In specific, for Tb12 in $Tb_{25}Co_{125}$, B_2^0, B_4^0, B_6^0, and B_6^6 are individually modified to be the same as those in $TbHCo_5$ while the other CFPs are fixed. As demonstrated in Figure S13, by comparison, the change of the E_{eigen} curve caused by hydrogen addition is mostly represented by the modification of B_2^0 term, whereas the variations of B_4^0, B_6^0, and B_6^6 exhibit negligible contributions. Figure S14 demonstrates a more direct comparison between E_{aniso} with negative and positive B_2^0 while leaving out all other higher-order terms. Here, we force the same magnitude of B_2^0 while changing the sign since the magnitude affects only the size of E_{aniso}. It shows a 90° reorientation of the easy magnetization axis from c to a axis in the simulated structure.

Evaluation of Strain Effect on Anisotropy Switching. Magnetoelastic effects may also be involved at the Pd/TbCo and TbCo/substrate interfaces due to hydrogen insertion. Hydrogen absorption in Pd layer induces lattice expansion up to 4%,[68] and subsequently, the TbCo layer can experience elastic strain. However, in our case, we want to emphasize that the thickness of the Pd layer is substantially smaller than that of TbCo layers. We have observed hydrogen-induced

anisotropy switching in Pd (2 nm)/TbCo (20 nm, 50 nm) layers, and the thickness of the Pd layer is only 2 nm in comparison with the 50 nm thickness of the TbCo layer. Hence, it is unlikely that the lattice expansion of Pd will affect the bulk anisotropy of the TbCo layer. Another direct evidence is that when the Pd layer was discharged by applying 0.2 V (desorption of hydrogen), magnetic anisotropy of the TbCo layer remained in-plane. This observation excludes the effect of lattice expansion in the Pd layer as the origin of anisotropy switching in amorphous TbCo.

We next consider the elastic strain between the TbCo layer and the substrate. The lattice volume of the TbCo layer may change much less upon hydrogen insertion due to large interstitial space in the amorphous structure.[69] Furthermore, the transfer of elastic strain between the substrate and thin films usually requires a high-quality interface (epitaxial growth of thin films) and a small thickness of thin films (for instance, below 10 nm). However, the conditions of our sputtering process, which was conducted at room temperature, resulted in a rough interface without epitaxial growth. The thickness of the TbCo layer, reaching 50 nm, further decreases the likelihood of a significant strain transfer. In addition, to better address the strain effect, we performed ab initio calculations to investigate the change of magnetic anisotropy using an elongated atomic structure along the *c* direction, which simulates the condition that the in-plane lattice is constrained, leaving only the out-of-plane degree of freedom. The strain level was set to 2% and 5% in the ab initio calculations, respectively. The results show that the magnitudes of crystal-field parameters (CFPs) are altered by around 0.001 eV (less than 5% of the CFPs before structural elongation) under strain up to 5%. As exemplified in Figure S16, the contour map of E_{aniso} demonstrates negligible changes due to the strain effect. All of these considerations and results lead us to believe that the strain effects may not play a substantial role in inducing anisotropy change.

AUTHOR INFORMATION

Corresponding Author

Xinglong Ye − *TUD-KIT Joint Research Laboratory Nanomaterials and Institute of Materials Science, Technische Universität Darmstadt, 64287 Darmstadt, Germany;* Present Address: School of Physics, Shandong University, 250100 Jinan, China; orcid.org/0000-0002-9515-4816; Email: xinglong.ye@tu-darmstadt.de

Authors

Zhengyu Xiao − *TUD-KIT Joint Research Laboratory Nanomaterials, Technische Universität Darmstadt, 64287 Darmstadt, Germany; Institute of Nanotechnology, Karlsruhe Institute of Technology, 76344 Eggenstein-Leopoldshafen, Germany; Key Laboratory of Magnetic Molecules and Magnetic Information Materials of Ministry of Education, School of Chemistry and Materials Science, Shanxi Normal University, Taiyuan 030032, China*

Ruiwen Xie − *Institute of Materials Science, Technische Universität Darmstadt, 64287 Darmstadt, Germany*

Fernando Maccari − *Institute of Materials Science, Technische Universität Darmstadt, 64287 Darmstadt, Germany;* orcid.org/0000-0002-4585-4179

Philipp Klaßen − *Faculty of Physics and Center for Nanointegration Duisburg-Essen (CENIDE), University of Duisburg-Essen, 47057 Duisburg, Germany*

Benedikt Eggert − *Faculty of Physics and Center for Nanointegration Duisburg-Essen (CENIDE), University of Duisburg-Essen, 47057 Duisburg, Germany;* orcid.org/0000-0001-7739-3541

Di Wang − *Institute of Nanotechnology, Karlsruhe Institute of Technology, 76344 Eggenstein-Leopoldshafen, Germany; Karlsruhe Nano Micro Facility, Karlsruhe Institute of Technology (KIT), 76131 Karlsruhe, Germany;* orcid.org/0000-0001-9817-7047

Yuting Dai − *Institute of Nanotechnology, Karlsruhe Institute of Technology, 76344 Eggenstein-Leopoldshafen, Germany*

Raquel Lizárraga − *Department of Materials Science and Engineering and Wallenberg Initiative Materials Science for Sustainability, KTH Royal Institute of Technology, SE-100 44 Stockholm, Sweden*

Johanna Lill − *Faculty of Physics and Center for Nanointegration Duisburg-Essen (CENIDE), University of Duisburg-Essen, 47057 Duisburg, Germany*

Tom Helbig – *Faculty of Physics and Center for Nanointegration Duisburg-Essen (CENIDE), University of Duisburg-Essen, 47057 Duisburg, Germany*
Heiko Wende – *Faculty of Physics and Center for Nanointegration Duisburg-Essen (CENIDE), University of Duisburg-Essen, 47057 Duisburg, Germany;* orcid.org/0000-0001-8395-3541
Kurt Kummer – *European Synchrotron Radiation Facility, F-38043 Grenoble, France*
Katharina Ollefs – *Faculty of Physics and Center for Nanointegration Duisburg-Essen (CENIDE), University of Duisburg-Essen, 47057 Duisburg, Germany*
Konstantin P Skokov – *Institute of Materials Science, Technische Universität Darmstadt, 64287 Darmstadt, Germany;* orcid.org/0000-0003-4321-9021
Hongbin Zhang – *Institute of Materials Science, Technische Universität Darmstadt, 64287 Darmstadt, Germany*
Zhiyong Quan – *Key Laboratory of Magnetic Molecules and Magnetic Information Materials of Ministry of Education, School of Chemistry and Materials Science, Shanxi Normal University, Taiyuan 030032, China; Collaborative Innovation Center for Shanxi Advanced Permanent Magnetic Materials and Technology, Research Institute of Materials Science, Shanxi Normal University, Taiyuan 030032, China;* orcid.org/0000-0002-8517-9622
Xiaohong Xu – *Key Laboratory of Magnetic Molecules and Magnetic Information Materials of Ministry of Education, School of Chemistry and Materials Science, Shanxi Normal University, Taiyuan 030032, China; Collaborative Innovation Center for Shanxi Advanced Permanent Magnetic Materials and Technology, Research Institute of Materials Science, Shanxi Normal University, Taiyuan 030032, China;* orcid.org/0000-0001-7588-4793
Robert Kruk – *Institute of Nanotechnology, Karlsruhe Institute of Technology, 76344 Eggenstein-Leopoldshafen, Germany*
Horst Hahn – *Institute of Nanotechnology, Karlsruhe Institute of Technology, 76344 Eggenstein-Leopoldshafen, Germany; School of Sustainable Chemical, Biological and Materials Engineering, University of Oklahoma, Norman, Oklahoma 73019, United States*
Oliver Gutfleisch – *Institute of Materials Science, Technische Universität Darmstadt, 64287 Darmstadt, Germany*

Author Contributions

Z.X. and R.X. contributed equally to this work. X.Y. conceptualized and supervised the work. Z.X. prepared thin films, conducted AHE and magnetometry measurements, and performed electrochemical measurements under the supervision of X.Y. R.X. and H.Z. carried out the DFT calculations. F.M. and X.Y. performed MOKE characterization. P.K., B.E., T.H., J.L., and K.K. performed the XMCD measurements at the ESRF, and P.K. and B.E. analyzed the XMCD data under the supervision of H.W. and K.O. Y.D. prepared TEM samples, and D.W. performed TEM characterizations. X.L. wrote the manuscript and coordinated the collaborations among the groups in KIT, TU Darmstadt, and the University of Duisburg-Essen. All authors contributed to the discussion of the results and the revision of the manuscript.

Notes

The authors declare no competing financial interest.

ACKNOWLEDGMENTS

RL thanks the Carl Tryggers Stiftelse for Vetenskaplig Forskning (CTS 22:2283) and the Åforsk Foundation (grant number 22-206), Sweden. XL acknowledges financial support by the Deutsche Forschungsgemeinschaft (DFG) under grant number 528530757. OG, KS, HZ, HW acknowledge financial support by the Deutsche Forschungsgemeinschaft (DFG) within the CRC/TRR270 (Project-ID 405553726). PK and BE acknowledge financial support from the German Federal Ministry of Education and Research (BMBF) under Grant BMBF-Projekt05K2022. We acknowledge the ESRF for the allocation of beam time at ID32 under proposal number IH-HC-3833 and the Karlsruhe Nano Micro Facility (KNMF). We also acknowledge the computing time provided at the NHR Center NHR4CES at RWTH Aachen University (project number p0020449) and at TU Darmstadt (project number p0020538). It is funded by the Federal Ministry of Education and Research and the state governments participating on the basis of the resolutions of the GWK for national high performance computing at universities.

REFERENCES

(1) Kim, S. K.; Beach, G. S.; Lee, K. J.; Ono, T.; Rasing, T.; Yang, H. Ferrimagnetic spintronics. *Nat. Mater.* **2022**, *21*, 24.
(2) Kim, K.-J.; Kim, S. K.; Hirata, Y.; Oh, S.-H.; Tono, T.; Kim, D.-H.; Okuno, T.; Ham, W. S.; Kim, S.; Go, G.; et al. Fast domain wall motion in the vicinity of the angular momentum compensation temperature of ferrimagnets. *Nat. Mater.* **2017**, *16*, 1187.
(3) Siddiqui, S. A.; Han, J.; Finley, J. T.; Ross, C. A.; Liu, L. Current-induced domain wall motion in a compensated ferrimagnet. *Phys. Rev. Lett.* **2018**, *121*, 057701.
(4) Zheng, Z.; Zhang, Y.; Lopez-Dominguez, V.; Sánchez-Tejerina, L.; Shi, J.; Feng, X.; Chen, L.; Wang, Z.; Zhang, Z.; Zhang, K.; et al. Field-free spin-orbit torque-induced switching of perpendicular magnetization in a ferrimagnetic layer with a vertical composition gradient. *Nat. Commun.* **2021**, *12* (1), 4555.
(5) Kim, D.-H.; Haruta, M.; Ko, H.-W.; Go, G.; Park, H.-J.; Nishimura, T.; Kim, D.-Y.; Okuno, T.; Hirata, Y.; Futakawa, Y.; et al. Bulk Dzyaloshinskii–Moriya interaction in amorphous ferrimagnetic alloys. *Nat. Mater.* **2019**, *18*, 685.
(6) Caretta, L.; Mann, M.; Büttner, F.; Ueda, K.; Pfau, B.; Günther, C. M.; Hessing, P.; Churikova, A.; Klose, C.; Schneider, M.; et al. Fast current-driven domain walls and small skyrmions in a compensated ferrimagnet. *Nat. Nanotechnol.* **2018**, *13*, 1154.
(7) Kim, C.; Lee, S.; Kim, H.-G.; Park, J.-H.; Moon, K.-W.; Park, J. Y.; Yuk, J. M.; Lee, K.-J.; Park, B.-G.; Kim, S. K.; et al. Distinct handedness of spin wave across the compensation temperatures of ferrimagnets. *Nat. Mater.* **2020**, *19* (19), 980.
(8) Stanciu, C. D.; Hansteen, F.; Kimel, A. V.; Kirilyuk, A.; Tsukamoto, A.; Itoh, A.; Rasing, T. All-optical magnetic recording with circularly polarized light. *Phys. Rev. Lett.* **2007**, *99*, 047601.
(9) Mangin, S.; Gottwald, M.; Lambert, C.-H.; Steil, D.; Uhlíř, V.; Pang, L.; Hehn, M.; Alebrand, S.; Cinchetti, M.; Malinowski, G.; et al. Engineered materials for all-optical helicity-dependent magnetic switching. *Nat. Mater.* **2014**, *13*, 286.
(10) Radu, I.; Vahaplar, K.; Stamm, C.; Kachel, T.; Pontius, N.; Dürr, H. A.; Ostler, T. A.; Barker, J.; Evans, R. F. L.; Chantrell, R. W.; et al. Transient ferromagnetic-like state mediating ultrafast reversal of antiferromagnetically coupled spins. *Nature* **2011**, *472* (472), 205.
(11) Chaudhari, P.; Cuomo, J. J.; Gambino, R. J. Amorphous metallic films for bubble domain applications. *IBM J. Res. Dev.* **1973**, *17* (17), 66.

(12) Hansen, P.; Clausen, C.; Much, G.; Rosenkranz, M.; Witter, K. Magnetic and magneto-optical properties of rare-earth transition-metal alloys containing Gd, Tb, Fe, Co. *J. Appl. Phys.* **1989**, *66* (66), 756.
(13) Coey, J. M. D. Hard magnetic materials: A perspective. *IEEE Trans. Magn.* **2011**, *47* (47), 4671.
(14) Gutfleisch, O.; Willard, M. A.; Brück, E.; Chen, C. H.; Sankar, S. G.; Liu, J. P. Magnetic materials and devices for the 21st century: Stronger, lighter, and more energy efficient. *Adv. Mater.* **2011**, *23* (23), 821.
(15) Patrick, C. E.; Kumar, S.; Balakrishnan, G.; Edwards, R. S.; Lees, M. R.; Petit, L.; Staunton, J. B. Calculating the magnetic anisotropy of rare-earth−transition-metal ferrimagnets. *Phys. Rev. Lett.* **2018**, *120* (120), 097202.
(16) Yang, Y.; Zhou, J.; Zhu, F.; Yuan, Y.; Chang, D. J.; Kim, D. S.; Pham, M.; Rana, A.; Tian, X.; Yao, Y.; et al. Determining the three-dimensional atomic structure of an amorphous solid. *Nature* **2021**, *592*, 60−64.
(17) Tian, H.; Ma, Y.; Li, Z.; Cheng, M.; Ning, S.; Han, E.; Xu, M.; Zhang, P.-F.; Zhao, K.; Li, R.; et al. Disorder-tuned conductivity in amorphous monolayer carbon. *Nature* **2023**, *615*, 56−61.
(18) Mizoguchi, T.; Cargill, G. S., III Magnetic anisotropy from dipolar interactions in amorphous ferrimagnetic alloys. *J. Appl. Phys.* **1979**, *50*, 3570−3582.
(19) Rooney, P. W.; Shapiro, A. L.; Tran, M. Q.; Hellman, F. Evidence of a Surface-Mediated Magnetically Induced Miscibility Gap in Co-Pt Alloy Thin Films. *Phys. Rev. Lett.* **1995**, *75*, 1843.
(20) Cheng, S.-N.; Kryder, M. H.; Mathur, M. C. A. Stress related anisotropy studies in DC-magnetron sputtered TbCo and TbFe films. *IEEE Trans. Magn.* **1989**, *25*, 4018.
(21) Harris, V. G.; Aylesworth, K. D.; Das, B. N.; Elam, W. T.; Koon, N. C. Structural origins of magnetic anisotropy in sputtered amorphous Tb-Fe films. *Phys. Rev. Lett.* **1992**, *69*, 1939.
(22) Harris, V. G.; Pokhil, T. Selective-resputtering-induced perpendicular magnetic anisotropy in amorphous TbFe films. *Phys. Rev. Lett.* **2001**, *87*, 067207.
(23) Fu, H.; Mansuripur, M.; Meystre, P. Generic source of perpendicular anisotropy in amorphous rare-earth-transition-metal films. *Phys. Rev. Lett.* **1991**, *66*, 1086.
(24) Yan, X.; Hirscher, M.; Egami, T.; Marinero, E. E. Direct observation of anelastic bond-orientational anisotropy in amorphous $Tb_{26}Fe_{62}Co_{12}$ thin films by x-ray diffraction. *Phys. Rev. B* **1991**, *43*, 9300.
(25) Matsukura, F.; Tokura, Y.; Ohno, H. Control of magnetism by electric field. *Nat. Nanotechnol.* **2015**, *10*, 209.
(26) Molinari, A.; Hahn, H.; Kruk, R. Voltage-control of magnetism in all-solid-state and solid/liquid magnetoelectric composites. *Adv. Mater.* **2019**, *31* (26), 1806662.
(27) Leighton, C. Electrolyte- ased ionic control of functional oxides. *Nat. Mater.* **2019**, *18*, 13.
(28) Tan, A. J.; Huang, M.; Avci, C. O.; Büttner, F.; Mann, M.; Hu, W.; Mazzoli, C.; Wilkins, S.; Tuller, H. L.; Beach, G. S. D. Magneto-ionic control of magnetism using a solid-state proton pump. *Nat. Mater.* **2019**, *18*, 35.
(29) Nichterwitz, M.; Honnali, S.; Kutuzau, M.; Guo, S.; Zehner, J.; Nielsch, K.; Leistner, K. Advances in magneto-ionic materials and perspectives for their application. *APL Mater.* **2021**, *9* (3), 030903.
(30) de Rojas, J.; Quintana, A.; Lopeandía, A.; Salguero, J.; Muñiz, B.; Ibrahim, F.; Chshiev, M.; Nicolenco, A.; Liedke, M. O.; Butterling, M.; et al. Voltage-driven motion of nitrogen ions: A new paradigm for magneto-ionics. *Nat. Commun.* **2020**, *11*, 5871.
(31) Tan, A.; Huang, M.; Avci, C. O.; Büttner, F.; Mann, M.; Hu, W.; Mazzoli, C.; Wilkins, S.; Tuller, H. L.; Beach, G. S. D. Magneto-ionic control of magnetism using a solid-state proton pump. *Nat. Mater.* **2019**, *18*, 35−41.
(32) Huang, M.; Hasan, M. U.; Klyukin, K.; Zhang, D.; Lyu, D.; Gargiani, P.; Valvidares, M.; Sheffels, S.; Churikova, A.; Büttner, F.; et al. Voltage control of ferrimagnetic order and voltage-assisted writing of ferrimagnetic spin textures. *Nat. Nanotechnol.* **2021**, *16*, 981.
(33) Ren, X.; Liu, L.; Cui, B.; Cheng, B.; Liu, W.; An, T.; Chu, R.; Zhang, M.; Miao, T.; Zhao, X.; et al. Control of Compensation Temperature in CoGd Films through Hydrogen and Oxygen Migration under Gate Voltage. *Nano Lett.* **2023**, *23*, 5927−5933.
(34) Tang, A.; Li, C.; Xu, T.; Dong, Y.; Ma, J.; Yu, P.; Nan, C.-W.; Lin, Y.-H.; Nan, T.; Jiang, W.; et al. *Nano Lett.* **2024**, *24*, 632−639.
(35) Ye, X.; Singh, H. K.; Zhang, H.; Geßwein, H.; Chellali, M. R.; Witte, R.; Molinari, A.; Skokov, K.; Gutfleisch, O.; Hahn, H.; et al. Giant voltage-induced modification of magnetism in micron-scale ferromagnetic metals by hydrogen charging. *Nat. Commun.* **2020**, *11*, 4849.
(36) Ye, X.; Yan, F.; Schäfer, L.; Wang, D.; Geßwein, H.; Wang, W.; Chellali, M. R.; Stephenson, L.; Skokov, K.; Gutfleisch, O.; et al. Magnetoelectric Tuning of Pinning-Type Permanent Magnets through Atomic-Scale Engineering of Grain Boundaries. *Adv. Mater.* **2021**, *33*, 2006853.
(37) Thórarinsdóttir, K. A.; Thorbjarnardóttir, B. R.; Arnalds, U. B.; Magnus, F. Competing interface and bulk anisotropies in Co-rich TbCo amorphous thin films. *J. Phys.: Condens. Matter* **2023**, *35*, 205802.
(38) El Hadri, M. S.; Hehn, M.; Pirro, P.; Lambert, C.-H.; Malinowski, G.; Fullerton, E. E.; Mangin, S. Domain size criterion for the observation of all-optical helicity-dependent switching in magnetic thin films. *Phys. Rev. B* **2016**, *94*, 064419.
(39) van Vucht, J. H. N.; Kuijpers, F. A.; Bruning, H. C. A. M. Reversible room-temperature absorption of large quantities of hydrogen by intermetallic compounds. *Philips Res. Rep.* **1970**, *25*, 133.
(40) Lewis, F. A. The hydrides of palladium and palladium alloys. *Platin. Met. Rev.* **1960**, *4*, 132.
(41) Ueda, K.; Mann, M.; de Brouwer, P. W. P.; Bono, D.; Beach, G. S. D. Temperature dependence of spin-orbit torques across the magnetic compensation point in a ferrimagnetic TbCo alloy film. *Phys. Rev. B* **2017**, *96*, 064410.
(42) Hubert, A.; Schäfer, R. *Magnetic domains: The analysis of magnetic microstructures*; Springer-Verlag: Berlin Heidelberg, 1998.
(43) Haltz, E.; Weil, R.; Sampaio, J.; Pointillon, A.; Rousseau, O.; March, K.; Brun, N.; Li, Z.; Briand, E.; Bachelet, C.; et al. Deviations from bulk behavior in TbFe(Co) thin films: Interfaces contribution in the biased composition. *Phys. Rev. Mater.* **2018**, *2*, 104410.
(44) Kummer, K.; Fondacaro, A.; Jimenez, E.; Velez-Fort, E.; Amorese, A.; Aspbury, M.; Yakhou-Harris, F.; Van Der Linden, P.; Brookes, N. B. The high-field magnet endstation for X-ray magnetic dichroism experiments at ESRF soft X-ray beamline ID_{32}. *J. Synchrotron Radiat.* **2016**, *234*, 64−73.
(45) Morales, F.; de Groot, F. M. F.; Glatzel, P.; Kleimenov, E.; Bluhm, H.; Hävecker, M.; Knop-Gericke, A.; Weckhuysen, B. M. In situ x-ray absorption of $Co/Mn/TiO_2$ catalysts for Fischer−Tropsch synthesis. *J. Phys. Chem. B* **2004**, *108*, 16201.
(46) de Groot, F. M. F.; Abbate, M.; van Elp, J.; Sawatzky, G. A.; Ma, Y. J.; Chen, C. T.; Sette, F. Oxygen 1s and Co 2p x-ray absorption of cobalt oxides. *J. Phys.: Condens. Matter* **1993**, *5*, 2277.
(47) López-Flores, V.; Bergeard, N.; Halté, V.; Stamm, C.; Pontius, N.; Hehn, M.; Otero, E.; Beaurepaire, E.; Boeglin, C. Role of critical spin fluctuations in ultrafast demagnetization of transition-metal rare-earth alloys V. *Phys. Rev. B* **2013**, *87*, 214412.
(48) Teramura, Y.; Tanaka, A.; Thole, B. T.; Jo, T. Effect of coulomb interaction on the x-ray magnetic circular dichroism spin sum rule in rare earths. *J. Phys. Soc. Jpn.* **1996**, *65*, 3056.
(49) Chen, C. T.; Idzerda, Y. U.; Lin, H.-J.; Smith, N. V.; Meigs, G.; Chaban, E.; Ho, G. H.; Pellegrin, E.; Sette, F. Experimental confirmation of the x-ray magnetic circular dichroism sum rules for iron and cobalt. *Phys. Rev. Lett.* **1995**, *75*, 152.
(50) Suzuki, D. H.; Valvidares, M.; Gargiani, P.; Huang, M.; Kossak, A. E.; Beach, G. S. D. Thickness and composition effects on atomic moments and magnetic compensation point in rare-earth transition-metal thin films. *Phys. Rev. B* **2023**, *107*, 134430.

(51) Cid, R.; Alameda, J. M.; Valvidares, S. M.; Cezar, J. C.; Bencok, P.; Brookes, N. B.; Díaz, J. Perpendicular magnetic anisotropy in amorphous Nd_xCo_{1-x} thin films studied by x-ray magnetic circular dichroism. *Phys. Rev. B* **2017**, *95*, 224402.
(52) Holmström, E.; Bock, N.; Peery, T. B.; Lizárraga, R.; De Lorenzi-Venneri, G.; Chisolm, E. D.; Wallace, D. C. Ab initio method for locating characteristic potential-energy minima of liquids. *Phys. Rev. E* **2009**, *80*, 051111.
(53) Lizárraga, R. Structural and magnetic properties of the Gd-based bulk metallic glasses $GdFe_2$, $GdCo_2$, and $GdNi_2$ from first principles. *Phys. Rev. B* **2016**, *94*, 174201.
(54) Novák, P.; Knížek, K.; Kuneš, J. Crystal field parameters with wannier functions: Application to rare-earth aluminates. *Phys. Rev. B* **2013**, *87*, 205139.
(55) Hellman, F.; Gyorgy, E. M. Growth-induced magnetic anisotropy in amorphous Tb-Fe. *Phys. Rev. Lett.* **1992**, *68* (9), 1391.
(56) Skomski, R.; Sellmyer, D. J. Anisotropy of rare-earth magnets. *J. Rare Earths* **2009**, *27*, 675.
(57) Pourovskii, L. V.; Boust, J.; Ballou, R.; Gomez Eslava, G.; Givord, D. Higher-order crystal field and rare-earth magnetism in rare-earth− Co_5 intermetallics. *Phys. Rev. B* **2020**, *101*, 214433.
(58) Avci, C. O.; Lambert, C.-H.; Sala, G.; Gambardella, P. Chiral coupling between magnetic layers with orthogonal magnetization. *Phys. Rev. Lett.* **2021**, *127*, 167202.
(59) Luo, Z.; Dao, T. P.; Hrabec, A.; Vijayakumar, J.; Kleibert, A.; Baumgartner, M.; Kirk, E.; Cui, J.; Savchenko, T.; Krishnaswamy, G.; et al. Chirally coupled nanomagnets. *Science* **2019**, *363*, 1435−1439.
(60) Ueno, T.; Inami, N.; Sagayama, R.; Wen, Z.; Hayashi, M.; Mitani, S.; Kumai, R.; Ono, K. Relation between electronic structure and magnetic anisotropy in amorphous TbCo films probed by x-ray magnetic circular dichroism. *J. Phys. D: Appl. Phys.* **2016**, *49*, 205001.
(61) Kresse, G.; Furthmuller, J. Efficient iterative schemes for ab initio total-energy calculations using a plane-wave basis set. *Phys. Rev. B* **1996**, *54*, 11169.
(62) Kuneš, J.; Arita, R.; Wissgott, P.; Toschi, A.; Ikeda, H.; Held, K. Wien2wannier: From linearized augmented plane waves to maximally localized Wannier functions. *Comput. Phys. Commun.* **2010**, *181* (11), 1888−1895.
(63) Mostofi, A. A.; Yates, J. R.; Pizzi, G.; Lee, Y.-S.; Souza, I.; Vanderbilt, D.; Marzari, N. An updated version of wannier90: A tool for obtaining maximally-localised Wannier functions. *Comput. Phys. Commun.* **2014**, *185* (8), 2309−2310.
(64) Blaha, P. WIEN2k, an augmented plane wave plus local orbital package for the electronic structure of solids. *Int. Tables Crystallogr.* **2024**, *ch. 6.22*, 836−842.
(65) Lu, Y.; Höppner, M.; Gunnarsson, O.; Haverkort, M. W. Efficient real-frequency solver for dynamical mean-field theory. *Phys. Rev. B* **2014**, *90*, 085102.
(66) Tripathi, S. *XMCD investigation at $M_{4,5}$ edges of the rare earth elements in high-performance permanent magnet*. PhD thesis, Devi Ahilya University 2018.
(67) Pourovskii, L. V.; Boust, J.; Ballou, R.; Gomez Eslava, G.; Givord, D. Erratum: Higher-order crystal field and rare-earth magnetism in rare-earth−Co_5 intermetallics [Phys. Rev. B 101 , 214433 (2020)]. *Phys. Rev. B* **2023**, *108*, 219905.
(68) Wagner, S.; Uchida, H.; Burlaka, V.; Vlach, M.; Vlcek, M.; Lukac, F.; Cizek, J.; Baehtz, C.; Bell, A.; Pundt, A. Achieving coherent phase transition in palladium-hydrogen thin films. *Scr. Mater.* **2011**, *64* (10), 978−981.
(69) Huang, L. J.; Lin, H. J.; Wang, H.; Ouyang, L. Z.; Zhu, M. Amorphous alloys for hydrogen storage. *J. Alloy. Comp.* **2023**, *941*, 168945.